RESEARCH ARTICLE

Key Points:
- Nearly synchronous and spatially uniform temperature increases were observed in the caldera of Axial Seamount during its 2015 eruption
- Numerical modeling supports the hypothesis that the 2015 temperature anomalies were caused by an eruption-related release of warm brines
- The 2015 temperature anomalies show the importance of water column monitoring to test models of the hydrothermal impacts due to eruptions

Supporting Information:
- Supporting Information S1
- Movie S1
- Movie S2
- Data Set S1

Correspondence to:
G. Xu,
guangyux@uw.edu

Observation and Modeling of Hydrothermal Response to the 2015 Eruption at Axial Seamount, Northeast Pacific

Guangyu Xu[1] (ID)**, William W. Chadwick Jr.[2]** (ID)**, William S. D. Wilcock[3]** (ID)**, Karen G. Bemis[4]** (ID)**, and John Delaney[3]**

[1]Applied Physics Laboratory, University of Washington, Seattle, WA, USA, [2]NOAA Pacific Marine Environmental Laboratory and Oregon State University, Newport, OR, USA, [3]School of Oceanography, University of Washington, Seattle, WA, USA, [4]Department of Marine and Coastal Sciences, Rutgers University, New Brunswick, NJ, USA

Abstract The 2015 eruption at Axial Seamount, an active volcano at a depth of 1500 m in the Northeast Pacific, marked the first time a seafloor eruption was detected and monitored by an in situ cabled observatory—the Cabled Array, which is part of the Ocean Observatories Initiative. After the onset of the eruption, eight cabled and noncabled instruments on the seafloor recorded unusual, nearly synchronous and spatially uniform temperature increases of 0.6–0.7°C across the southern half of the caldera and neighboring areas. These temperature signals were substantially different from those observed after the 2011 and 1998 eruptions at Axial and hence cannot be explained by emplacement of the 2015 lava flows on the seafloor. In this study, we investigate several possible explanations for the 2015 temperature anomalies and use a numerical model to test our preferred hypothesis that the temperature increases were caused by the release of a warm, dense brine that had previously been stored in the crust. If our interpretation is correct, this is the first time that the release of a hydrothermal brine has been observed due to a submarine eruption. This observation would have important implications for the salt balance of hydrothermal systems and the fate of brines stored in the subsurface. The observation of the 2015 temperature anomalies and the modeling presented in this study also demonstrate the importance of contemporaneous water column observations to better understand hydrothermal impacts of submarine eruptions.

1. Introduction

Approximately 80% of the Earth's volcanic output takes place in the oceans (Crisp, 1984), yet most of those eruptions go undetected because they occur at great depths and out of the range of most existing monitoring systems. Previous observations of seafloor eruptions and studies of their impacts have primarily relied on fast-response cruises dispatched upon detection of an event and follow-up field expeditions (Baker et al., 2012; Rubin et al., 2012). The logistical demand of cruise organization limits the response time to a few weeks or months, and hence, observational data recorded during an eruption and its immediate aftermath have remained scarce. In recent years, the advent of two cabled observatories on the Juan de Fuca Ridge has greatly advanced our means of detecting and monitoring seafloor eruptions (Kelley et al., 2014). The permanent presence of a cabled observatory allows unprecedented long-term real-time monitoring of seafloor volcanic activities. In April 2015, an eruption began at Axial Seamount, which is the largest volcanic edifice on the Juan de Fuca Ridge in the Northeast Pacific; that eruption was recorded by instruments on the Ocean Observatories Initiative Cabled Array (OOI-CA), which had been operational since fall 2014. When the April 2015 eruption started, the real-time data recorded by the observatory instruments allowed researchers, for the first time, to monitor a seafloor volcanic event as it happened. The multidisciplinary data recorded by observatory and autonomous instruments revealed with unprecedented detail the seismic, hydroacoustic, geodetic, and geological characteristics of the eruption (Caplan-Auerback et al., 2017; Chadwick et al., 2016; Clague et al., 2017; Levy et al., 2018; Nooner & Chadwick, 2016; Spietz et al., 2018; Wilcock et al., 2016).

In this paper, we show that a nearly synchronous and uniform bottom water temperature increase was recorded by eight observatory and autonomous instruments across the southern half of the caldera and neighboring areas soon after the onset of the 2015 eruption at Axial Seamount. After considering various possible causal mechanisms for the temperature signal, we hypothesize that the eruption triggered the

release of a hydrothermal brine that had been previously stored in the crust. In this interpretation, the observed temperature increases were due to a dense, bottom-hugging layer of warm salty water that was created when hot brines in the crust were flushed out when the 2015 dike intersected the zone where the brines were stored. In the absence of near-bottom salinity observations, we test the feasibility of this hypothesis by using a numerical model of ocean circulation and transport to simulate the thermal response within the vicinity of the caldera following a brine release. The results suggest that this may be the first time that the release of a hydrothermal brine has been observed due to a submarine eruption.

2. Recent Eruptions at Axial Seamount

Axial Seamount is located where the Cobb hotspot is superimposed on the Juan de Fuca Ridge, approximately 500 km from the Oregon coast (Chadwick et al., 2005; Embley et al., 1990). The volcano has a summit at 1,420-m depth, a 3-km by 8-km horseshoe-shaped caldera with walls up to 140-m high and a floor at 1,510- to 1,580-m depth and is flanked by north and south trending rift zones (Figure 1a). The co-location of an oceanic spreading center with the Cobb hotspot leads to an enhanced magma supply that makes Axial the most active submarine volcano in the Northeast Pacific with more than 52 eruptions over the past 800 years (Clague et al., 2013). Since monitoring and mapping of Axial started in the mid-1980s, three eruptions have been confirmed including the latest one in 2015. The first documented eruption occurred in January 1998 (Embley et al., 1999). Seismic unrest associated with the eruption started at the summit and a dike then migrated southward over 50 km to reach the end of the south rift zone (SRZ; Dziak & Fox, 1999). Subsequent seafloor mapping showed the 1998 lava flows erupted along the SE edge of the caldera and upper SRZ (Chadwick et al., 2013; left panel in Figure 1b). Axial erupted again in these same areas in April 2011, which initially went undetected and was later confirmed based on seafloor observations and data recorded by autonomous monitoring instruments (Caress et al., 2012; Chadwick et al., 2012; Dziak et al., 2012). The 2011 eruption also produced a large pillow lava ridge 30 km down the SRZ in addition to lava flows along the SE edge of the caldera and the upper SRZ (Clague et al., 2017; middle panel in Figure 1b).

In April 2015, the onset of the eruption was evident in real time when OOI-CA observatory monitoring instruments showed increased seismicity along the eastern edge of the caldera at ~5:00 UTC on 24 April (Wilcock et al., 2016) followed by large tilt signals and deflation of the caldera floor at 6:00 UTC (Nooner & Chadwick, 2016). In contrast to the previous two eruptions, the most voluminous and thickest of the 2015 lava flows were erupted along the north rift zone (NRZ), 8–16 km north of the summit caldera (Chadwick et al., 2016). Seafloor mapping also revealed thinner lava flows on the NE caldera floor and on the north caldera rim (Clague et al., 2017; right panel in Figure 1b). During the eruption, seismometers and hydrophones installed on the OOI-CA recorded numerous impulsive hydroacoustic signals originating from the locations of the lava flows (Wilcock et al., 2016). Inspection of contemporaneous seismometer and hydrophone data suggests those impulsive signals were due to lava-water interactions [Caplan-Auerbach et al., 2017; Chadwick et al., 2016; Wilcock et al., 2016].

3. Post-2015 Eruption Bottom Temperature Anomalies

Following the onset of the 2015 eruption, eight observatory and autonomous instruments distributed across the southern half of the caldera and its neighboring areas (Figure 2) registered a nearly synchronous and uniform 0.6–0.7°C temperature increase that started approximately 3 days after the eruption began and lasted for ~40 days (Figure 3a). Those eight instruments included three cabled bottom pressure recorders (BPRs), four uncabled BPRs (Nooner & Chadwick, 2016; Sasagawa et al., 2016), and one 3-D thermistor array on the OOI-CA observatory (Figure 2). The seven BPRs span a distance ~3-km east-west and ~5-km north-south across the southern half of the caldera and its SE rim. Each BPR contained a temperature sensor inside the pressure housing that recorded background temperature. The 3-D thermistor array, consisting of 24 thermistors attached to a triangular wire frame of approximately 0.5 m on each side, was deployed in the ASHES vent field at the SW corner of the caldera to measure the 3-D temperature distribution of diffuse flow hydrothermal discharge (see Figure S1 in supporting information). The array consists of four layers with the top one extending to approximately 80 cm above the seafloor.

The 2015 temperature signals were fundamentally different in character from the temperature anomalies observed after the 1998 and 2011 eruptions (Figure 3). During those two previous eruptions, the
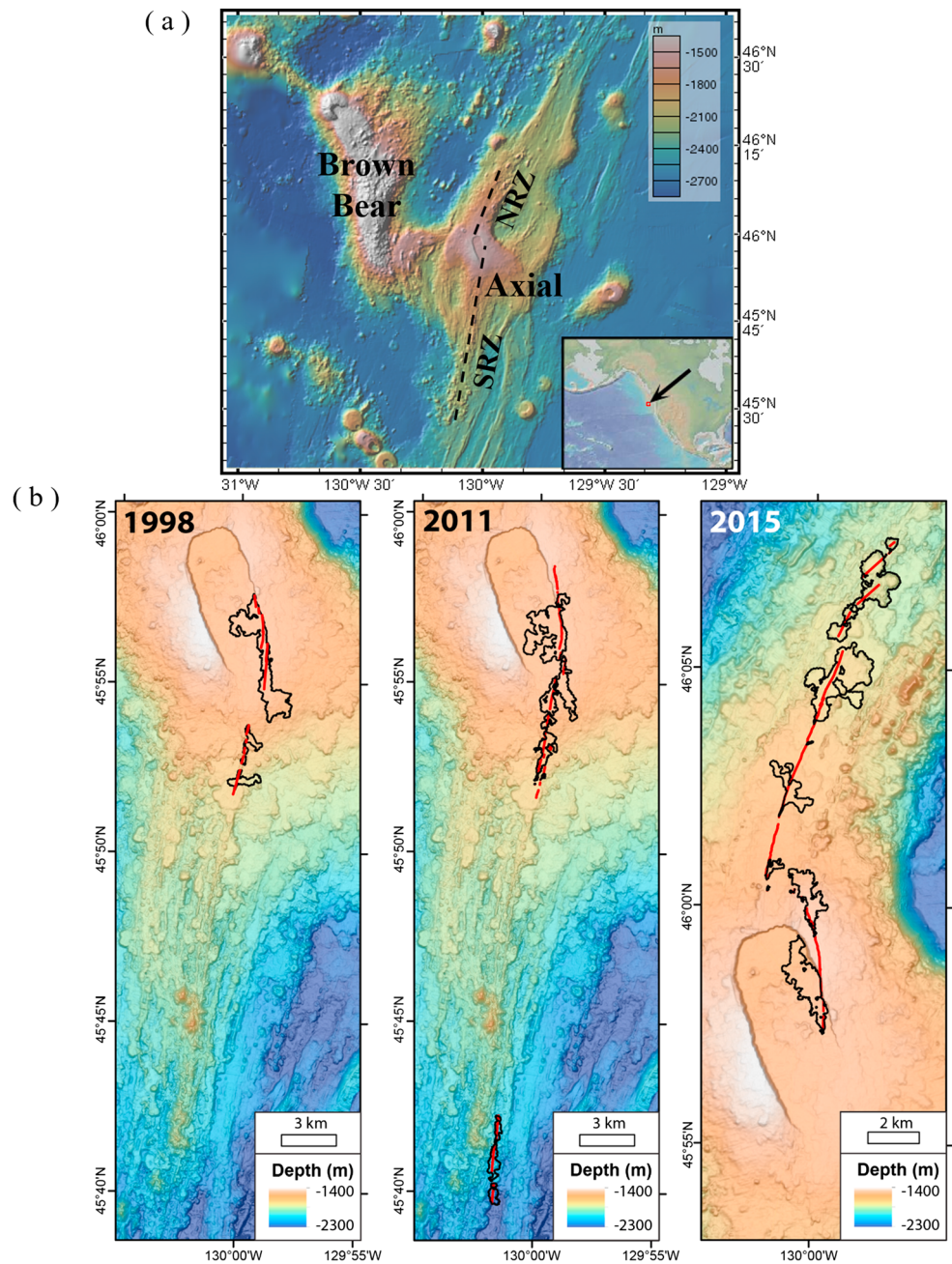
Figure 1. (a) Bathymetry of Axial Seamount and the adjacent Brown Bear Seamount. The dashed lines mark the trends of the north rift zone (NRZ) and the south rift zone (SRZ). (b) Bathymetry of the summit of axial seamount and the outlines of the lava flows (black) from the 1998 (left, after Chadwick et al., 2013), 2011 (middle, after Caress et al., 2012 and Clague et al., 2017), and 2015 (right, after Clague et al., 2017) eruptions. The red lines mark the eruptive fissures.

temperature increases recorded by BPRs in the caldera (Figures 3b and 3c) began within 6–18 hr after the onset of major deflation, and had maximum amplitudes of 0.2–0.5°C above ambient (except for the 2.8°C temperature increase recorded by the BPR-south instrument (Figure 3c), which was caught in the 1998 lava flow (Fox et al., 2001). The previous temperature increases also peaked within the first 24 hr and declined sharply thereafter (Figures 3b and 3c). In addition, the temperature spikes fluctuated between elevated and ambient levels on time scales of hours, presumably due to tidal-induced changes in bottom currents, and were incoherent between sites located 2–3 km apart (Chadwick et al., 2012; Chadwick & Nooner, 2015;
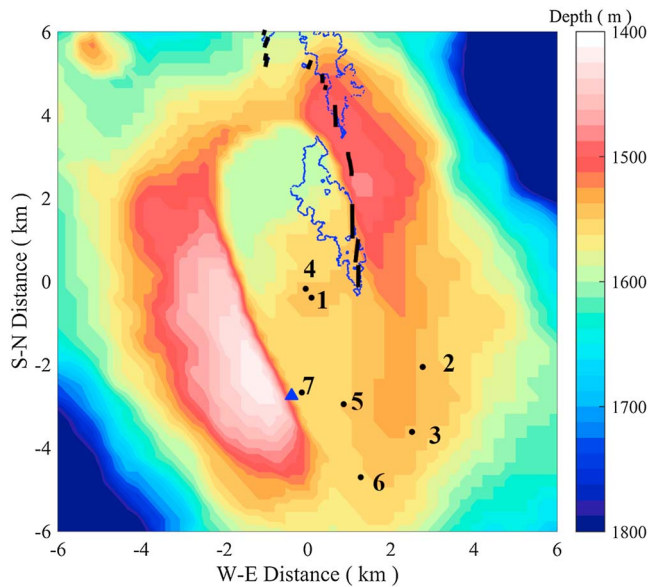
Figure 2. Bathymetry of the summit caldera of Axial Seamount. The black dots mark the locations of three observatory bottom pressure recorders (BPRs): Central Cal. (1), East Cal. (2), Int. Dist. (3), and four autonomous BPRs: BPR-C (4), BPR-S1 (5), BPR-S2 (6), and SCPR (7). The blue triangle marks the location of the 3-D thermistor array deployed at the ASHES vent field (with an offset of 100-m westward from its true location for graphical clarity). The blue lines show the outlines of the lava flows from the 2015 eruption and the thick black lines mark the eruptive fissures (after Chadwick et al., 2016 and Clague et al., 2017).

Fox, 1999). In sharp contrast, the 2015 temperature increase (Figure 3a) began later (~3 days after deflation started), had a higher maximum amplitude above ambient (0.6–0.7°C), did not peak until ~18 days after the start of the increase, and featured a bell-shaped pattern in time that had a much longer duration (~40 days) before returning to background levels. Perhaps the most striking and significant difference is the spatial and temporal coherence of the temperature increases in 2015 over the entire southern half of the caldera and its SE rim (Figures 2 and 3a). The near-synchronous temporal patterns and the normal background variability of the temperature signals make it difficult to determine if there is a directionality to the onset of the temperature increases (in other words whether they started in the north and moved south, for example).

The 1998 and 2011 temperature anomalies were interpreted to be caused by recently erupted lava flows on the seafloor near the BPR instruments (Chadwick et al., 2012; Fox, 1999; Fox et al., 2001). During those two previous eruptions, the lava flows reached within 100 to 600 m of the BPRs, with the exception of one BPR being caught in the 1998 lava flow (Fox et al., 2001). The interpretation was that plumes of warmed water rising from the lava flows were wafted back and forth over the BPRs on the seafloor, driven by oscillatory bottom currents, which led to the short-term fluctuations of the temperature signals. In comparison, the 2015 lava flows were 1 to 4 km away from the BPRs and the thermistor array, yet the temperature signals were larger. This, combined with the spatial and temporal extent and coherence of the temperature increases in 2015, suggests that the nearby lava flows were unlikely to be the cause of the temperature anomalies.

4. Possible Explanations of the 2015 Seafloor Temperature Anomalies

Possible explanations for the temperature increases in 2015 include the following: (1) diffuse venting increased almost everywhere throughout the southern caldera for a time after the 2015 eruption, (2) a plume of warm water was created from the eruption of the thickest lava flows on Axial's north rift zone, which rose up, became neutrally buoyant, and then drifted southward and blanketed the caldera, (3) a plume of warm water that blanketed the caldera was created by Hawaiian-style fire-fountaining in and near the caldera as part of the 2015 eruptive activity, and (4) the release of a hydrothermal brine that blanketed the seafloor. Below, we consider the first three explanations in turn and show why none of them seem to be a likely explanation for the 2015 temperature signals and then in the next section evaluate the brine release hypothesis in detail.

4.1. Wide-Spread Eruption-Related Increase of Diffuse Venting

Perhaps the simplest possible explanation for the 2015 temperature increases is that the eruption caused an increase in diffuse hydrothermal venting almost everywhere throughout the southern caldera. However, this idea is not supported by available evidence, including spatially extensive remotely operated vehicle (ROV) and submersible visual observations. The first problem is that this has not happened during previous eruptions. The hydrothermal response to the 1998 and 2011 eruptions was limited to the heat coming off the cooling lava flows, and their underlying feeder dikes, especially within about 50–100 m of the eruptive fissures where snowblower vents were concentrated (Chadwick et al., 2013; Meyer et al., 2013). In addition, the hydrothermal vents at Axial are localized along the caldera faults and along the rift zones (Butterfield et al., 2004; Embley et al., 1990). There has never been any evidence of venting at the center of the caldera, which is visited frequently to perform ROV-based pressure measurements (Nooner & Chadwick, 2016), and this was true after the 2015 eruption as well—there was no evidence of increased diffuse hydrothermal venting except on the still-cooling 2015 lava flows (Chadwick et al., 2016; Clague et al., 2017). Similarly, the 3-D array thermistors that where most influenced by the local (ASHES) diffuse hydrothermal venting experienced a decrease in temperature even while the neighboring thermistors (<1-m distance) with the least venting influence experienced the increase in temperature as shown in Figure 3a (see Figure S2 in the supporting information).
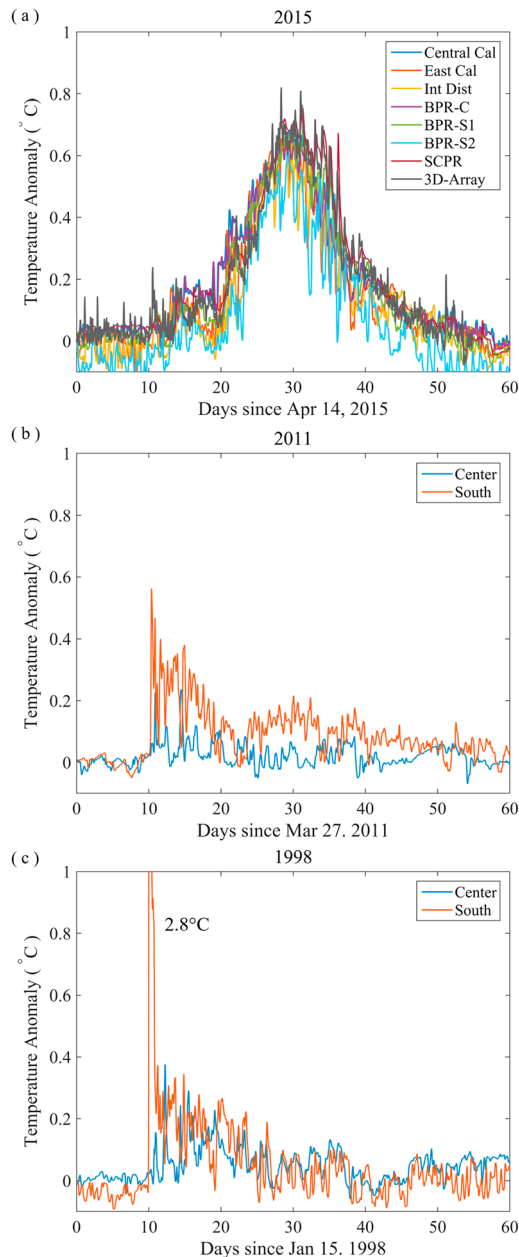
Figure 3. Near-bottom temperature anomalies recorded during eruptions at Axial Seamount in (a) 2015, (b) 2011, and (c) 1998. For each record, the original data was first averaged with a 2-hr moving window to remove high-frequency oscillations. Subsequently, the temperature anomaly was calculated for each record by subtracting a reference temperature recorded 10 days before the onset of the eruption (24 April 2015, 6 April 2011, and 25 January 1998) from the moving average. The 2015 temperature anomalies were recorded by seven bottom pressure recorders (BPRs) and the 3-D thermistor array, whose locations are marked in Figure 2. For the 3-D thermistor array, the data shown are from a thermistor that recorded near-ambient temperature with minimal perturbation by diffuse flow venting before the eruption. In 2011 and 1998, the temperature data were recorded by two BPRs located in the central and southern caldera, located near BPRs 1 and 5 in Figure 2, respectively. The peak value of the temperature anomaly recorded by the BPR in the southern caldera in 1998 (labeled in c) is clipped at 1°C. The large temperature increase was a result of that BPR being caught in the 1998 lava flow (see Fox et al., 2001).

4.2. Warm Plumes From Thick 2015 Northern Lava Flows

During the 2015 eruption, the most voluminous and thickest lava flows came out along the NRZ (Chadwick et al., 2016; Clague et al., 2017), 8- to 16-km north of the summit caldera (Figure 1b). Another possible explanation for the temperature increases in the caldera is that the eruption of the thickest NRZ lava flows caused enough hydrothermal venting to generate a plume of warm water that rose upward into the water column, became neutrally buoyant at the depth of Axial's summit, and then drifted southward and blanketed the caldera. The depth of the southern caldera floor is about 200–300 m above the thickest NRZ lava flows. There is evidence for extensive hydrothermal venting on the thick NRZ lava flows from visual observations during ROV dives in August 2015, 4 months after the eruption (Chadwick et al., 2016) and from conductivity-temperature-depth (CTD) tow-yos conducted at the same time that observed hydrothermal plumes ~100 m over the NRZ lava flows (Spietz et al., 2018).

However, physical oceanographic considerations question whether a plume from the NRZ lava flows would have a temperature anomaly that was high enough to match the magnitude (~0.6–0.7°C) of the observed temperature increases and would also be at the right depth to blanket the caldera. The scaling analysis of Speer and Rona (1989) suggests that the temperature anomaly of a neutrally buoyant plume is proportional to the plume's rise height off the bottom. To evaluate this hypothesis, we used an integral plume model to derive the temperature-plume-height relationship based on the ambient ocean stratification observed near Axial Seamount. The plume model was adapted from the one described in Xu and Dilorio (2012). We replaced the linear equation of state in the original Xu and Dilorio model with a hybrid equation of state that calculates density and other thermodynamic properties of plume fluids using the TEOS-10 thermodynamic equation of seawater (McDougall & Barker, 2011) for fluids with temperatures <40°C and a thermodynamic equation of NaCl solution (Driesner, 2007) for fluids with temperatures >40°C. The model also explicitly solves the conservation equations of enthalpy and salinity. We obtained the ambient temperature and salinity profiles used in the model by fitting quadratic curves to the hydrographic data from a *background* CTD cast collected 35 km to the NE of Axial in August 2015 (away from any effects of the eruption) between depths of 900 m and 2,100 m.

We conducted several sets of simulations using the integral plume model with different source and background settings. In the *base* set of simulations, we used $\Delta T = 300°C$, $\Delta S = 0$ ppt $U = 0.3$ m/s, where ΔT and ΔS are the temperature and salinity anomalies of the vent source fluid and U is the initial exit flow rate of the fluid. We adjusted the area of the vent source so that its heat flux varied from 100 MW to 30 GW in 500 MW increments. The vent source was at 1,840-m depth, which corresponds to the depth of the deepest NRZ lava flow discovered after the 2015 eruption. After each simulation was finished, we recorded the terminal plume height (Z_t), where the vertical velocity of the plume became zero and the simulation was terminated, and the temperature anomaly (ΔT_e) at the equilibrium plume height (Z_e), where the plume density first became equal to the ambient seawater density. Note that $Z_t > Z_e$, because a plume will rise past Z_e driven by its residual vertical momentum. During this *overshoot*, the plume becomes negatively buoyant and eventually stops rising at Z_t where the vertical momentum vanishes. Subsequently, the plume settles down, oscillates,

AGU
100
ADVANCING EARTH
AND SPACE SCIENCE

Geochemistry, Geophysics, Geosystems
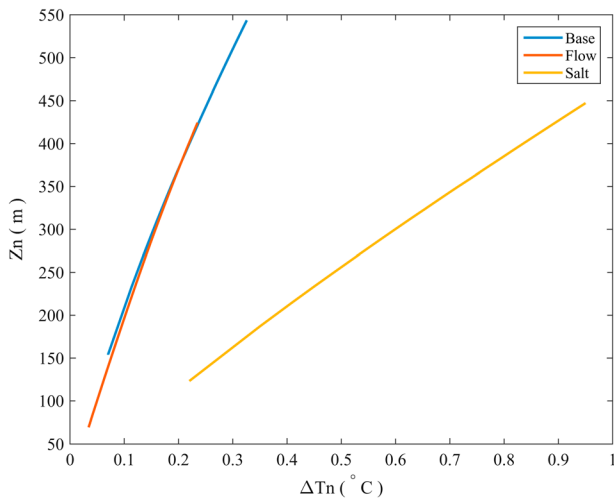
10.1029/2018GC007607

Figure 4. Integral plume model estimates of neutral plume height (Zn) versus temperature anomaly (ΔT) from three simulations, referred to in the text as *base* (blue), *flow* (red), and *salt* (yellow). See text for explanation.

and eventually disperses horizontally around an intermediate level between Zt and Ze, which we call the neutral plume height (Zn). Note that Zn > Ze, because while the plume overshoots and then settles down, it mixes with lighter seawater above Ze and hence reaches neutral buoyancy at a higher level with a reduced density. According to Tao et al. (2013), the ratio Zn/Zt ~ 0.92, which was used to obtain Zn from the model estimates of Zt. In addition, the plume temperature anomaly (ΔTn) at Zn is smaller than ΔTe. This is because as the plume overshoots and then settles down, it mixes with fresher ambient seawater above Ze, which reduces the salinity anomaly of the plume and hence the temperature anomaly at neutral buoyancy. Because the integral plume model cannot simulate the settling of the plume, we used ΔTe as a proxy for ΔTn, which results in its overestimation. As the following discussion shows, this overestimation does not affect the conclusions of our analysis.

The model results from the base simulations (blue line in Figure 4) show that ΔTn increases with Zn, which is consistent with the scaling analysis of Speer and Rona (1989). For a plume that originated from the NRZ lava flows and dispersed at 300 m above the bottom at the level of Axial's caldera, the estimated plume temperature anomaly is 0.15°C. On the other hand, as projected from the model results (beyond the axes limits in Figure 4), a plume having a temperature anomaly of 0.6°C to 0.7°C would disperse at 800 to 855 m above the NRZ lava flows or >500 m above Axial's caldera. Because the model overestimates temperature anomaly (see discussion above), the actual plume height would have been even larger. This result suggests that it is unlikely a plume with the characteristics in our base simulation that originated from the NRZ lava flows and dispersed at the level of Axial's caldera could have a temperature anomaly high enough to match the magnitude of the observed temperature increases.

The model results above are for a plume rising in a quiescent environment with no ambient flow. Previous studies suggest the presence of background cross flow can enhance a plume's mixing with ambient seawater and hence reduce the plume's rise height (Xu & DiIorio, 2012). To investigate the sensitivity of our model results to ambient flows, we conducted a second set of simulations, referred to as *flow*, which had the same base source conditions but with a spatially uniform horizontal flow of 0.1 m/s added to the background. The results suggest that the temperature-plume-height relationship is not significantly different from the base result (red curve in Figure 4), despite the reduced Zn and Tn with respect to a given source heat flux.

When a plume becomes neutrally buoyant, its temperature and salinity anomalies balance each other so that the plume's density equals that of ambient seawater. Therefore, the temperature-plume-height relationship is also sensitive to the plume's salinity, which is primarily a function of the ambient salinity stratification and the plume's source salinity anomaly. To investigate the sensitivity of our model results to the latter, we conducted a third set of model simulations, referred to as *salt*, with zero ambient cross flow and the same base source conditions except for a nonzero source salinity anomaly of $\Delta S = 30$ ppt. The results show a substantial increase of Tn at a given Zn relative to the *base* value (yellow curve in Figure 4). As a result, the plume height corresponding to Tn = 0.6–0.7°C has reduced to 300–343 m, which brackets the vertical distance between the deepest NRZ lava flow and Axial's caldera. Therefore, a vent source at the NRZ lava flows could conceivably produce a plume that reached neutral buoyancy at the level of Axial's caldera with a temperature anomaly high enough to match the observed temperature increases, but only if the source fluids had a high enough salinity anomaly. We also tested the sensitivity of our model results to source temperature anomalies and flow rates. The results (see Figure S3 in supporting information) show negligible effects of those two parameters on the temperature-plume-height relationship.

Overall, the integral model results suggest it is unlikely for a warm plume originating from the NRZ lava flows to have caused the observed temperature increases inside Axial's caldera, unless either (1) the plume was from a source located >800 m below the caldera or (2) the plume source had a substantially higher salinity than ambient seawater. Furthermore, the size and dispersion trajectory of the plume and its interaction with the ambient ocean circulation around Axial would need to have allowed the plume to be transported

southward and blanket Axial's summit caldera for over a month. The influence of the background circulation around the summit of Axial Seamount will be considered below in sections 6 and 7.

4.3. Warm Plumes From Hawaiian-Style Fountaining During the 2015 Eruption

Caplan-Auerbach et al. (2017) described *prolonged diffuse broadband acoustic signals* that were observed by hydrophones at Axial during the 2015 eruption between 1 and 20 May and interpreted them to be caused by *Hawaiian explosive or degassing eruptive activity* in or near the caldera, citing as evidence the ash that was observed on some seafloor benchmarks in the caldera. They also speculated that ash-laden plumes may have caused the temperature increases seen by the BPRs. We believe this alternative explanation is unlikely for the following reasons.

Ash was indeed observed on some of the benchmarks used for pressure measurements in the southern caldera (Clague et al., 2018; Nooner & Chadwick, 2016), which are located near the BPRs shown in Figure 2 that measured the temperature increases. However, the distribution of the ash is highly variable on those benchmarks, being thickest on the northern most benchmark (near BPRs 1 and 4 in Figure 2), falling off rapidly with distance southward, and being absent from the southern most benchmarks (near BPRs 3 and 6 in Figure 2). Chadwick et al. (2016) interpreted that the ash came from the 2015 eruptive vents that fed the lava flow on the NE floor of the caldera (Figure 2), because the ash is thickest nearest those eruptive fissures and decreases with distance away from them, the NE caldera lava flow morphology suggests it was emplaced with a high effusion rate over a short duration (hours-days), and because the chemical composition (MgO) of the ash matches the NE caldera lava flow (and not the NRZ lava flows). Caplan-Auerbach et al. (2017) suggest that the diffuse sounds indicate explosive degassing or ash eruption which could have produced the 0.7°C temperature rise seen by the BPRs. But if an ash laden, bottom-hugging plume raised the temperature, then why did it not deposit ash on all the benchmarks equally even though the temperature increase was similar at all the BPRs? Also, ash-laden plumes would presumably come and go with waxing and waning of the eruptive activity (the diffuse acoustic sounds are intermittent) and would result in fluctuating temperatures, not the long-duration, bell-shaped pattern recorded by the BPRs. In addition, if *Hawaiian explosive activity* had occurred after the NE caldera lava flow was emplaced, there would be evidence for such activity along the eruptive fissures in the form of substantial ash and spatter deposits on top of the lava flow where this degassing occurred, but no such deposits have been observed by post-eruption ROV dives in the area.

The timing is also problematic. The impulsive explosions recorded by the OOI-CA seismometers during the 2015 eruption described by Wilcock et al. (2016) show the duration of lava flow emplacement at various sites during the 2015 eruption. The locations of these explosions with time show that the eruption started first in the NE caldera on 24 April and activity only lasted there for a few days. The NRZ lava flows started later but lasted longer, until about 20 May. The timing of the diffuse acoustic signals described by Caplan-Auerbach et al. (2017) is between 1 and 20 May, which suggests that they also came from the NRZ, not from inside the caldera (which had already shut off by then). This makes them harder to relate to the temperature signals inside the caldera.

The BPR data show the rate of deflation decreased exponentially during the eruption (Nooner & Chadwick, 2016). The rate of deflation is related to the rate that lava is being withdrawn from the summit reservoir and must also be roughly proportional to the rate that lava is being erupted onto the seafloor. Ninety percent of the deflation was complete within the first 24 hr of the eruption. This is the time when eruption rates were likely highest (and the NE caldera lava flow was emplaced) and when the ash was most likely produced (since it has the same composition). After 1 May the rate of deflation was much lower, and it is more difficult to envision vigorous Hawaiian eruptive activity or explosive degassing during the waning stages of the eruption.

5. Preferred Hypothesis: Release of Hydrothermal Brine During the 2015 Eruption

It has long been evident that phase separation occurs in subsurface hydrothermal circulation cells, which can result in the formation of high-salinity brines and low-salinity vapors (Bischoff & Rosenbauer, 1989). The buoyancy contrast between the vapor and brine phases leads to their physical segregation. The vapor phase, driven by its buoyancy, upwells, and eventually vents at the seafloor. The brine phase, by contrast, is denser and so is harder to vent and is more likely to be stored in the crust. Bischoff and Rosenbauer (1989) proposed a two-layer model in which dense brines produced from phase separation accumulate at the base of a
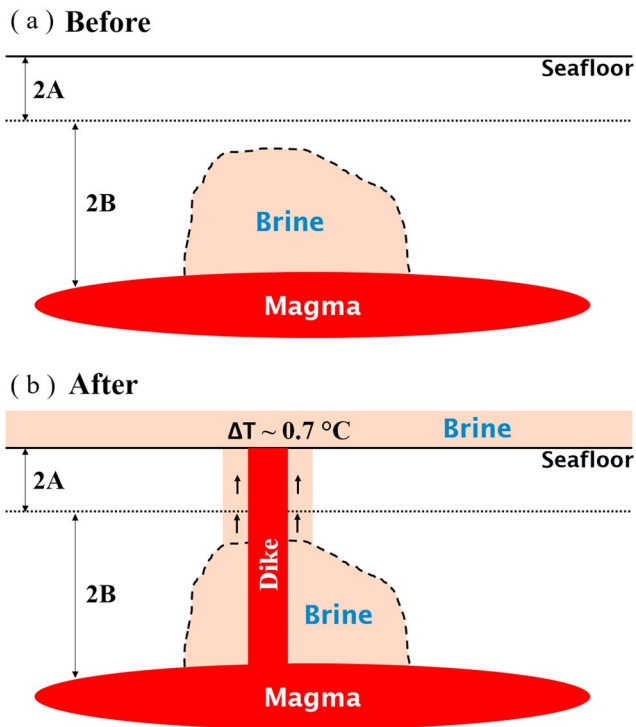
(a) **Before**

(b) **After**

Figure 5. (a) Conceptual diagram of a localized brine reservoir (tan) that had existed beneath axial caldera before its 2015 eruption. The black dashed curve delimits the outline of the brine reservoir. The black dotted line marks the layer 2A/2B interface. (b) At the onset of the eruption in 2015, we hypothesize that a dike injection (red) released brines from the subsurface reservoir, which led to the ~0.6–0.7°C near-bottom temperature increase observed across the southern half of the caldera and its neighboring areas. The arrows denote the rising brines through the brecciated rock adjacent to the dike walls.

hydrothermal system. The brine layer is initially stratified but double-diffusion processes eventually break up the stratification and initiate convection. Superimposed on the brine layer is another convective circulation cell of seawater in the single-phase regime. The convection of seawater is driven by the conductive heat transfer through a thin interface atop the brine layer. In a later study, Fontaine and Wilcock (2006) investigated the dynamics of the brine layer proposed by Bischoff and Rosenbauer (1989) and concluded that convection of brines is unlikely to occur and a stratified brine layer would have to be unreasonably thin to support the high hydrothermal heat flux observed at the Endeavor Segment of the Juan de Fuca Ridge. Fontaine and Wilcock (2006) then proposed an alternative model, in which both brines and vapors produced from phase separation are initially buoyant under the cold-hydrostatic pressure gradients in the hydrothermal system and hence upwell in its upflow zone. However, because brines are denser, rising brines preferentially fill small fissures, dead ends, and backwater porosity while the vapor phase flows efficiently through major conduits and eventually vents at the seafloor. In this model, the storage of brines is not restricted to the base of a hydrothermal system but likely extends from the top of the magma chamber upward into layer 2B. The layer 2A/2B interface is likely an upper limit of brine storage due to the decrease in pressure gradients that occurs as fluids enter the higher permeability Layer 2A (Fontaine & Wilcock, 2006).

There is clear evidence at Axial Seamount for boiling of hydrothermal fluids in the subsurface and phase separation (Butterfield et al., 1990; Butterfield et al., 1997). In addition, most of the hydrothermal vents at Axial have salinities lower than seawater (D. Butterfield, personal communication, March 1, 2018). This *salt deficit* implies the storage of brines beneath the seafloor, which could lead to the formation of subsurface brine reservoirs as envisioned by Fontaine and Wilcock (2006). Instead of being uniformly distributed above the magma chamber, we envision those reservoirs would likely be localized and semi-isolated in layer 2B (Figure 5).

We envision that during the 2015 eruption, the dike punctured through such a brine reservoir as it rose from the magma reservoir to the seafloor (Figure 5). In this model, the heat and gas released from the magma in the dike could substantially increase the buoyancy of the brines adjacent to the dike (Cann & Strens, 1989). In addition, the propagation of the dike would brecciate the adjacent country rock creating new cracks and faults (Lowell & Germanovich, 1995), which can serve as conduits for brines to reach the seafloor driven by the buoyancy gained from heat and gas injection from the magma. This is similar to one hypothesized formation mechanism of *megaplumes*, which are large volumes of heated, buoyant hydrothermal fluids injected high up in the water column and associated with eruptions (Baker et al., 1987; Baker et al., 1995; Baker et al., 2011; Murton et al., 2006). Similarly, we hypothesize that a massive release of brines from subsurface reservoirs occurred during the 2015 eruption of Axial Seamount. However, instead of forming a buoyant plume, the high-salinity brines formed a bottom-hugging layer of warm fluids that filled the caldera, which led to the observed widespread near-bottom temperature increase (Figure 3a).

A natural question arising from this hypothesis is the following: if brines rose to the seafloor driven by the buoyancy gained from heating and gas injection from dike emplacement, how could they then overcome their buoyancy to form a dense, bottom-hugging layer on the seafloor instead of a rising plume? The answer to this question is that an initially buoyant brine can become negatively buoyant when the brine mixes with ambient seawater, because of the nonlinear temperature-density relationship of brines at high temperatures (Turner & Campbell, 1987). For example, at a pressure of 150 bar, a 350°C brine with a salinity of <36 wt. % NaCl is buoyant relative to background seawater at 2°C and 3.4 wt. % NaCl. As this brine mixes with ambient seawater, the density of the mixture increases as the brine-to-seawater ratio decreases. Because of the nonlinear temperature-density relationship, the density of the brine-seawater mixture will exceed the density of seawater and hence buoyancy reversal will occur, if the initial brine salinity is sufficiently high
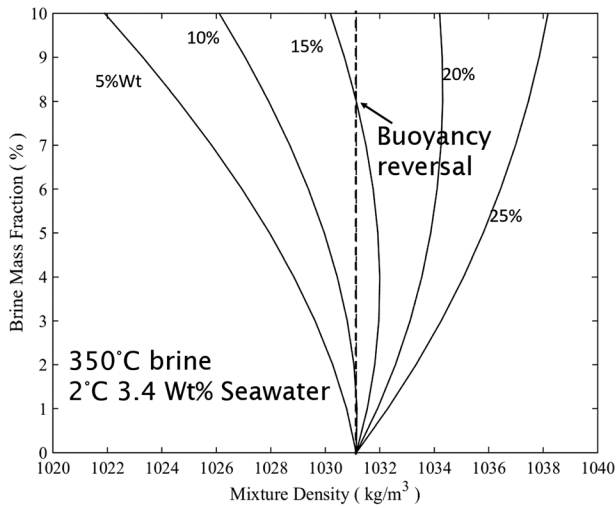
Figure 6. Density of a brine-seawater mixture versus the mass fraction of brine in the mixture. The ambient seawater has a temperature of 2°C and a salinity of 3.4 wt. %. The brine has an initial temperature of 350°C. The initial salinities of the brine are labeled on the curves in wt. %.

(Figure 6). According to Turner and Campbell (1987), the minimal initial salinity for a 350°C brine to reverse buoyancy is ~7.2 wt. % NaCl. Therefore, a 350°C brine with an initial salinity between 7.2 wt. % and 36 wt. % NaCl will undergo buoyancy reversal as the brine mixes with ambient seawater. The numerical study of Choi and Lowell (2015) predicts salinities of the end-member brines formed in the basal reaction zone of a hydrothermal system to be 30–50 wt. % NaCl. Therefore, brines having salinities within the aforementioned buoyancy-reversal range can form in the subsurface as mixtures between end-member brines and low-salinity ambient pore fluids. Driven by their buoyancy, those brines will vent at the seafloor but will ultimately settle back to the bottom after reaching the buoyancy-reversal point through dilution (Figure 6). On the other hand, brines having salinities lower than the minimum required for buoyancy-reversal will stay buoyant and rise to form a plume that reaches neutral buoyancy and disperses at a distance above the seafloor. This would fit one of the conditions for the warm plume hypothesis discussed in section 4.2 that requires a high-salinity plume source. The hypothesis of a plume that originated from the NRZ lava flows would then be another form of the water column expression of brine release from the subsurface.

6. Numerical Model

In the absence of near-bottom salinity measurements on the summit of Axial Seamount during its 2015 eruption, we test the hypothesis discussed in the preceding section by using a numerical model of ocean circulation and transport to simulate the thermal response within the vicinity of Axial caldera following a brine injection. This model can at least test if the idea of brine release causing the observed temperature anomalies is physically feasible or not. The model used in this study was initially constructed to study the ocean circulation, hydrography, and transport around Axial Seamount (Xu & Lavelle, 2017). The model domain covers a ~100 by 100 km region centered at Axial (Figure 7a). The domain is open to flow on all four
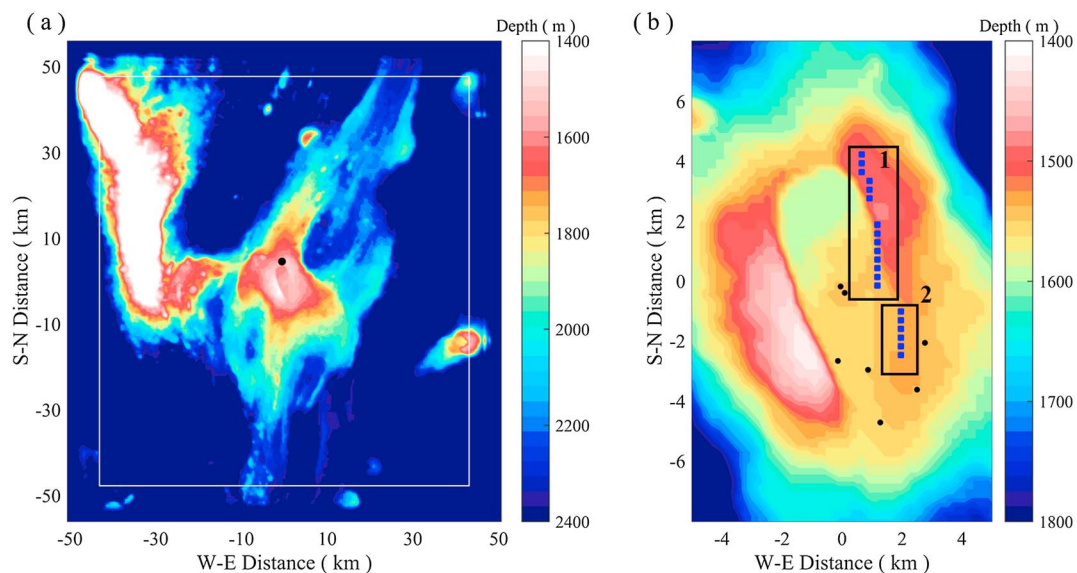

Figure 7. (a) Bathymetry within the model domain. The white line marks the inner edge of the *pretty good sponge* zone used to absorb the waves generated in the model interior. The back dot marks the location of a current meter at 950-m depth, whose data where used to derive the forcing used to drive flow in the model. (b) Bathymetry of the caldera of axial. The blue squares mark the locations of 20 bottom cells with prescribed heat and salt fluxes that represent the brine sources in the model and correspond to some of the 2011 and 2015 eruptive fissures (in boxes labeled 2 and 1, respectively). The black dots mark the locations of the seven bottom pressure recorders. The coordinate origin is at 45.958°N, 130.010°W.

sides with a layer of the *pretty good sponge* developed by Lavelle and Thacker (2008) padded along the inner edge of the boundary to absorb the outgoing baroclinic waves originating from the interior of model domain (Figure 7a). The model uses a stretched grid with resolution decreasing from the domain center to the boundaries. In horizontal directions, the model cell size grows parabolically from 262 by 290 m near the center of the caldera to 651 by 721 m near domain boundaries. In the vertical direction, the cell thickness increases from 13 m at 1,400-m depth to 43 m near the sea surface and the deepest points of the domain. The model uses gridded bathymetry data around Axial Seamount acquired from the Global Multi-Resolution Topography Synthesis of Marine Geoscience Data System (http://www.marine-geo.org/tools/GMRTMapTool). The model uses measured hydrography profiles as initial conditions for temperature and salinity. The flow in the model starts from zero and is driven by the time-dependent forcing derived from current meter measurements made above Axial Seamount at 950-m depth in June–August 2002 using the iterative force finding procedures described in Lavelle et al. (2010) and Xu and Lavelle (2017) (location of current meter shown in Figure 7a).

In the model, we prescribed heat and salt fluxes for 20 bottom cells that represent the sources of brine fluids (Figure 7b). Each bottom cell has a horizontal area of ~260 by 290 m and a vertical thickness of ~13 m. The locations of the northernmost 14 cells (inside box 1 in Figure 7b) coincide with the 2015 eruptive fissures on the NE caldera floor and the NE caldera rim as mapped by Chadwick et al. (2016) and Clague et al. (2017). This is consistent with the hypothesis that brine release was caused by the 2015 dike intersecting a subsurface brine reservoir, and the brine rose adjacent to the dike and exited the seafloor near where the dike reached the surface. The locations of the southernmost six cells (inside box 2 in Figure 7b) follow the southward subsurface propagation of the 2015 dike inferred from co-eruption seismicity and deformation (Nooner & Chadwick, 2016; Wilcock et al., 2016). The total linear distance of brine sources spans 7 km. Such placement of brine sources is consistent with the idea that dike injection leads to a substantial increase in crustal permeability near the dike walls (Lowell & Germanovich, 1995) along which brines can preferentially flow upward. In the model, the brine sources were turned on for 30 days following an initial 10-day spin-up of the model ocean circulation. The source intensity was ramped up linearly from zero to a maximum over a 15-day period followed by a linear decline back down to zero over 15 days, reflecting the steady increase and decrease in the observed temperature anomalies (Figure 3a). The maximum source heat and salt fluxes in the model are 0.02 MW/m^2 and 0.67 g/s/m^2, respectively. We did not attempt to directly simulate the initial rise of brines and their descent toward the seafloor after the buoyancy reversal discussed in section 5. This is because the hydrostatic assumption in our model is likely inappropriate for simulating density-driven flows with large vertical accelerations associated with the initial rise and fall of brines. Furthermore, the equation of state used in the model does not resolve the nonlinear temperature-density relationship at high temperatures and hence the buoyancy reversal of brines. Instead, we assume the buoyancy reversal occurs within the 13-m thick bottom cells of the model and the horizontal advection of brines during their initial rise and descent is negligible. Based on this assumption, the start of brine release in our model corresponds to the moment right after brines are deposited onto the seafloor following buoyancy reversal. Therefore, the brines released in our model are initially negatively buoyant relative to ambient seawater and remain so throughout a simulation. The total amount of heat and salt released are 3.1×10^{16} J and 1.3×10^9 kg. We conducted a separate simulation without heat and salt sources to investigate the background circulation pattern at Axial in the absence of the brine release.

7. Model Results

7.1. The General Pattern of Ocean Circulation at Axial Seamount

After an initial 10-day spin-up, the model results show that ocean circulation averaged over a 29.5-day (i.e., one lunar cycle) period following the brine release features an anticyclonic (clockwise) toroidal circulation around the summit of Axial with a maximum speed of 10–11 cm/s at a depth of 1,500 m (Figure 8a). Xu and Lavelle (2017) attributed the presence of the clockwise circulation around Axial to the rectification of oscillatory flows at tidal and subtidal frequencies. Within the caldera, mean flow is from north to south in general with inflow from the northern end of the caldera and outflow at its southern end (Figure 8a). These flow patterns are similar to the results obtained from the reference simulation wherein the brine source is turned off. The most noticeable difference between the model run with brine release and the one without is the flow inside the caldera. At 1,500-m depth, when the brine source is on, the
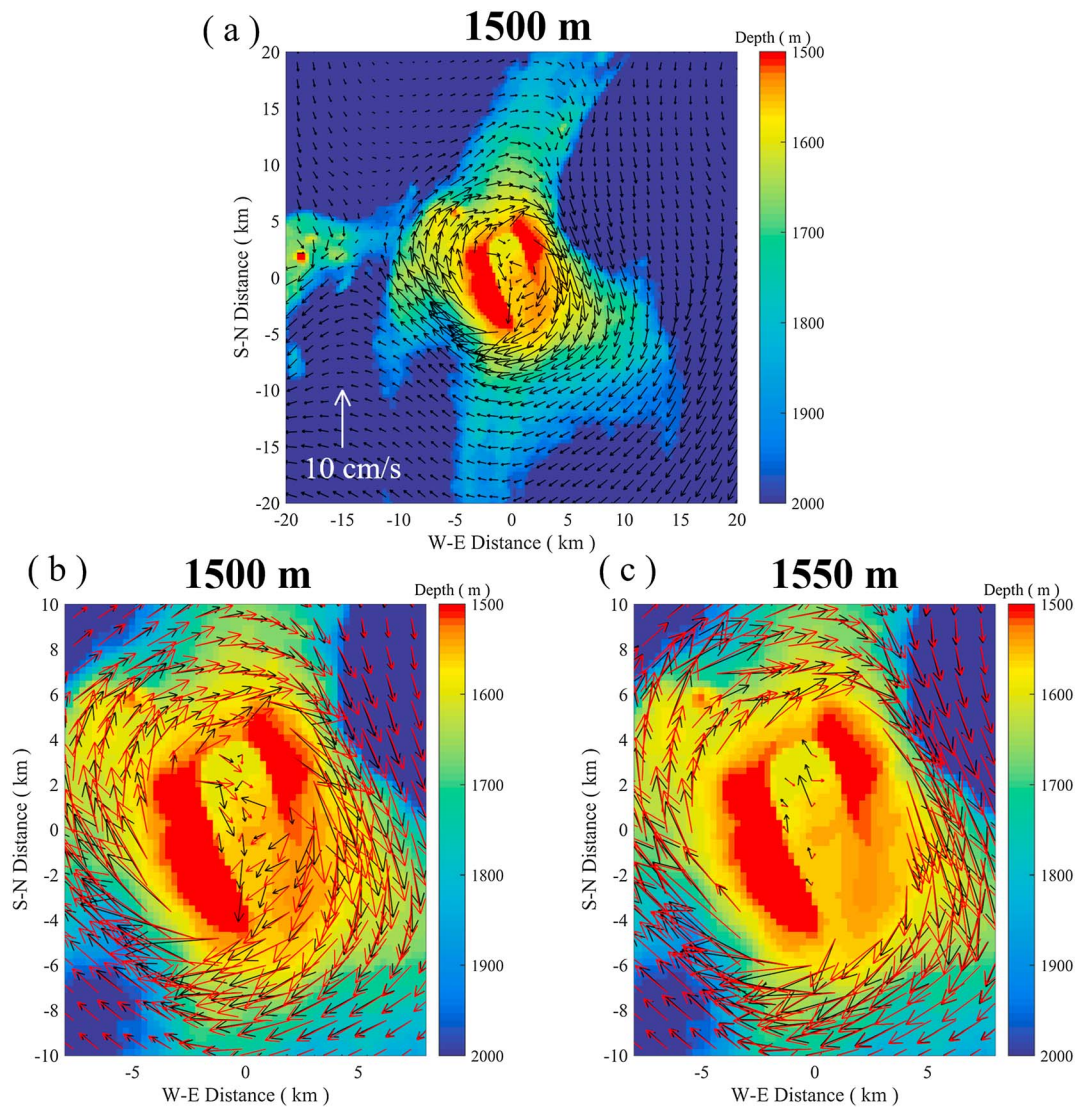
Figure 8. (a) Model velocity vectors at 1,500-m depth averaged over a 29.5-day period constrained using current meter data beginning 1 July 2002. The coordinate origin is the same as in Figure 7. Release of brines starts at the beginning of the 29.5-day period. (b) Comparison between 29.5-day averaged flows at 1,500-m depth obtained from the simulations with (black arrows) and without (red arrows) the release of brines. (c) Same as (b) except at 1,550-m depth.

direction of the flow near the southern end of the western caldera wall shifts from west-southwest to south-southwest, steered by the outflow of dense brines from the caldera in that region, which simultaneously draws flow into the caldera from the east where the caldera wall is the lowest (Figure 8b). At 1,550-m depth, which is deeper than most of the caldera floor except for the bowl-shaped topographic depression in the north, the flow becomes stronger and shifts northward when the brine source is on, which reflects the flow of dense brine toward the deeper northern end of the caldera (Figure 8c). These comparisons suggest the release of dense brines drives near-bottom currents and significantly alters the prerelease circulation inside the caldera.

7.2. Model Results of Bottom Temperature and Salinity Anomalies

The model results show the brine-induced near-bottom temperature, and salinity anomalies gradually occupy the entire caldera and its SE rim during the period when the brine is released from the seafloor (Figure 9). By day 15 after the start of brine release, a temperature anomaly of 0.7°C and a salinity anomaly of 0.15 ppt cover almost the entire caldera (Figures 9e and 9f). The animations of near-bottom temperature and salinity anomalies (Movies S1 and S2 in the supporting information) show that dense brine fluids exit the
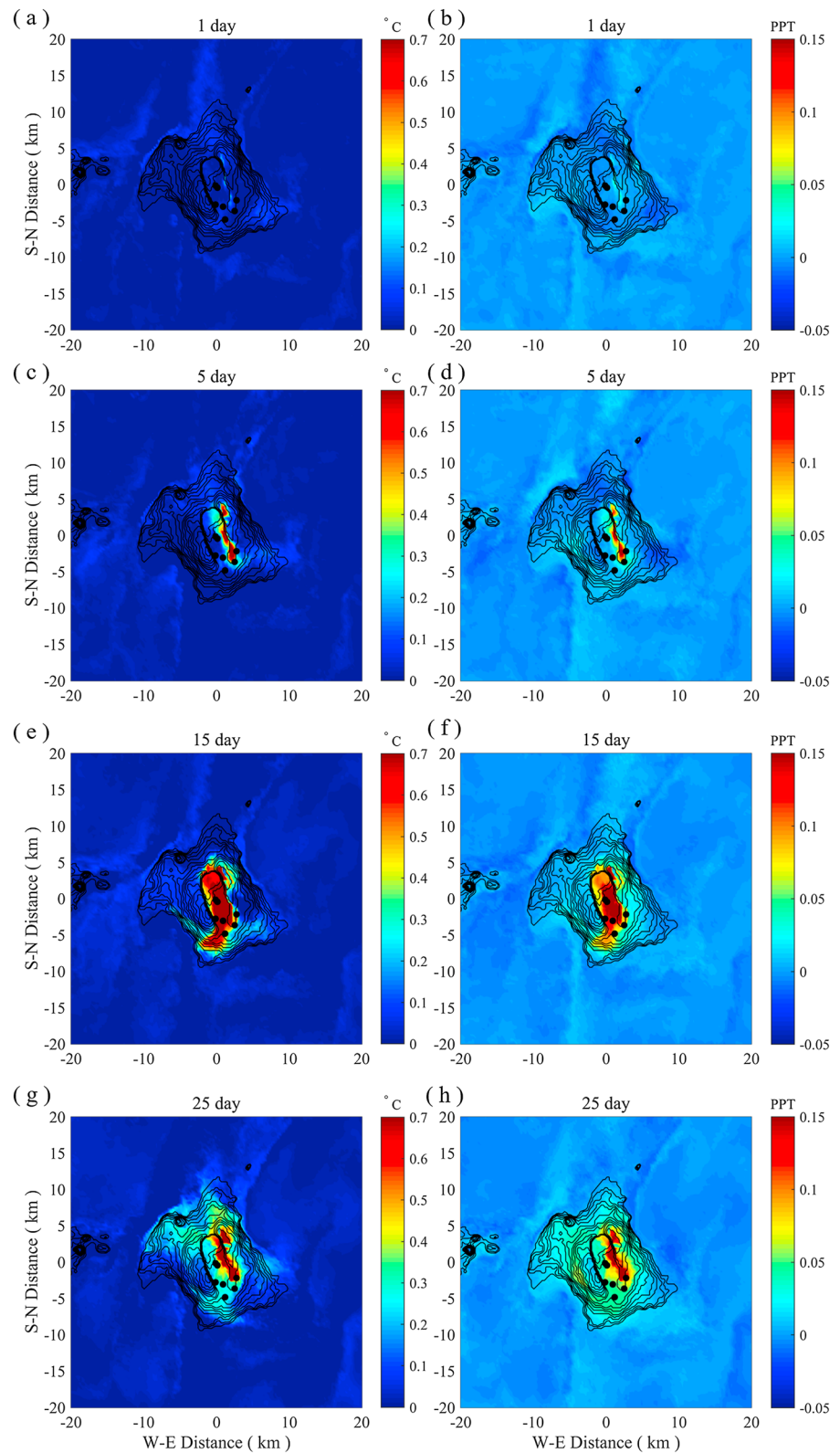
Figure 9. Model near-bottom temperature (left) and salinity (right) anomalies at 1 day (a and b), 5 days (c and d), 15 days (e and f), and 25 days (g and h) after the start of brine release. The black dots mark the locations of seven bottom pressure recorders. See also Movies S1 and S2 in the supporting information.
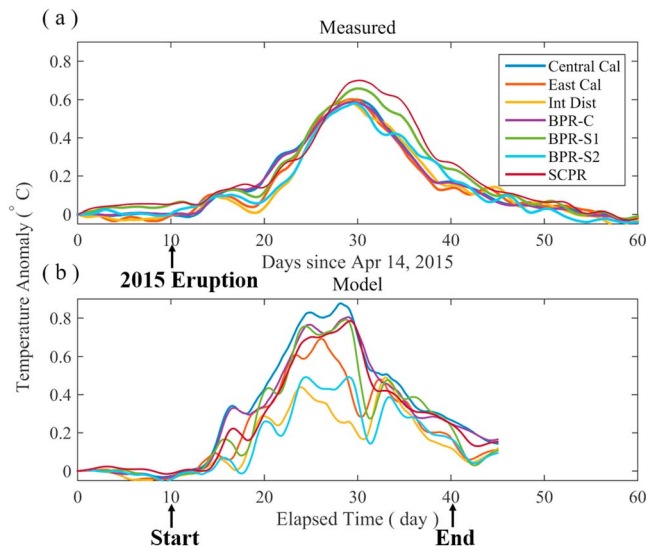
Figure 10. Observed (a) and model (b) near-bottom temperature anomalies at the locations of the seven bottom pressure recorders (BPRs) marked in Figure 2. The observed and model data were averaged with a moving 2-day window to remove high-frequency (e.g., tidal) oscillations. The anomalies were then calculated by subtracting the initial temperature from each record. The time of the start (10 day) and end (40 day) of brine release in the model and the 2015 eruption is labeled.

caldera from its southern and northern ends driven by episodic southward and northward currents inside the caldera respectively. Once outside the caldera, the dense brines flow downhill over the flanks and then circulate the summit in a clockwise direction driven by the toroidal flow around Axial (Figure 8a). The temperature and salinity anomalies then gradually decrease as the brine source starts to ramp down after day 15 (Figures 9g and 9h), and the anomalies all but disappear by the end of the simulation period (see Movies S1 and S2 in supporting information).

The near-bottom temperature anomalies sampled in the model at the locations of the seven BPRs (Figure 10b) show several of the key characteristics of the 2015 observations (Figure 10a). First, the magnitude of the temperature anomaly is close to 0.6–0.7°C at most of the BPR sites (Table 1). Second, the temperature anomalies are relatively coherent, both spatially and temporally, between the seven BPR measurement sites. Third, those anomalies rise and fall in a bell-shaped pattern with time. However, there are also some differences between the model and observed temperatures. The synthetic temperature anomalies do not have as much spatial coherency as the observed temperatures, and there is more spread in the model temperature records between sites (Figure 10b). The largest temperature increases are at the two central caldera BPR sites: Central Cal and BPR-C, where the model overestimates the temperature increase by 0.28°C and 0.22°C, respectively (Table 1). The smallest temperature increases are at the southernmost two sites: Int Dist and BPR-S2, the BPRs that are farthest away from the brine sources, where the model underestimates the temperature increase by ~ 0.1°C (Table 1). In addition, the model temperature anomalies overall have larger oscillations than the observations, which indicate that the model might overestimate the near-bottom oscillatory flows on Axial's summit. Also, the synthetic temperature anomalies rise and peak sooner than the observations. This difference is primarily due to the specific choices of model brine source parameters in the simulation (onset timing, duration, temporal variation of source fluxes). Those parameters could be tuned to achieve a better match between the synthetic temperature anomalies and the observations. We elected not to do so, because the primary goal of our simulations is to reproduce the magnitudes and overall temporal and spatial pattern of the observed temperature increases to test the brine release hypothesis, rather than achieve as close a match with the observations as possible.

Despite these differences, the model results show that temperature anomalies like those observed after the 2015 eruption could conceivably be produced by the release of a hydrothermal brine along the eruptive fissures and the area of dike intrusion along the eastern side of the caldera. Some of the mismatch between the model results and the observations could be explained by limitations in the model approach, as explained below.

8. Discussion
8.1. Numerical Model Limitations

Some limitations of the model and uncertainties of its parameters can affect the model outputs and potentially contribute to the mismatch between the simulated and observed temperature anomalies (Figure 10). First, the bottom model cells on the summit of Axial are 13-m thick, which determines the minimum thickness of the simulated near-bottom brine layer. In comparison, the real brine layer would only need to be a few meters thick to generate the observed temperature increases since the eight recording instruments (seven BPRs plus the 3-D thermistor array)

Table 1
Magnitudes of the Observed and Model Near-Bottom Temperature Anomalies at the Locations of the Seven Bottom Pressure Recorders (BPRs) Marked in Figure 2

Site name	Observed (°C)	Model I (°C)	Model II (°C)	Model III (°C)
Central Cal	0.60	0.88	0.79	0.82
East Cal	0.60	0.69	0.41	0.53
Int Dist	0.59	0.49	0.27	0.37
BPR-C	0.59	0.81	0.69	0.72
BPR-S1	0.66	0.79	0.72	0.65
BPR-S2	0.58	0.49	0.44	0.42
SCPR	0.70	0.78	0.60	0.56

Note. The observed and model data were averaged with a moving 2-day window to remove high-frequency (e.g., tidal) oscillations. Three sets of model results are included: Model I is the main simulation described in the text; Model II has the same setting as the main simulation except that the vertical resolution was doubled and the brine heat and salt fluxes were reduced by half (Figure S4 in the supporting information); Model III has the same setting as the main simulation except that the forcing was derived from the currents measured above Axial at 950-m depth in August–September 2001 (a different time period from the same current meter data set used in Model I) (Figure S5 in the supporting information).

were all less than 1 m above the bottom. Therefore, the volume of brine released in the model—in the form of heat and salt fluxes—could be an overestimate of the actual volume of brine released on Axial's summit that caused the observed temperature increases following the 2015 eruption. To investigate the sensitivity of our model results to bottom cell thickness, we doubled the vertical resolution to reduce the bottom cell thickness to 7 m and reduced the heat and salt fluxes from brine sources by half in a separate simulation. The resulting temperature anomalies sampled at the seven BPR sites (see Figure S4 in the supporting information and Table 1) have similar magnitudes and overall temporal pattern of increase and decrease as the observations. This suggests that the amount of heat and salt needed to generate the observed 0.6°C to 0.7°C temperature anomalies in the model are proportional to the height of the bottom cells in the model.

Second, the forcing used to drive the background flow in the model was derived from the current meter measurements recorded in 2002. Obviously, it would be best to have current data recorded during the 2015 eruption, but in the absence of such data the 2002 data set can constrain important aspects of the circulation pattern at Axial Seamount, in particular the presence of the clockwise toroidal flow (Figure 8a). Furthermore, the release of dense brines will significantly alter the circulation inside the caldera and make it less dependent on the large-scale background flow (Figures 8b and 8c). To test the sensitivity of model results to background forcing, we conducted a separate simulation using the forcing derived from the currents measured above Axial at 950-m depth in August–September 2001 (a different time period from the same current meter data set), when the overall direction of background flow shifted from southwest to west. This separate simulation yielded near-bottom temperature anomalies of similar magnitudes and overall trends at the locations of the seven BPRs (Figure S5 in the supporting information and Table 1).

Third, the model used in this study is a hydrostatic one and hence may not be able to sufficiently resolve density-driven flows with large vertical accelerations. Since the initial rise of brines and their descent following buoyancy reversal are neglected in the model, strong vertical motions primarily occur when brines flow down the flanks after exiting the caldera. Let L and h be the characteristic horizontal and vertical length scales associated with the downhill motions of brines with characteristic horizontal and vertical velocities U and W. According to Marshall et al. (1997), the nonhydrostatic effects are negligible if

$$\frac{U^2}{L^2N^2} << 1, \tag{1}$$

where N is the buoyancy frequency of ambient seawater. Using $N = 0.0014$ rad/s, which is calculated from the CTD data collected between 1,400- and 2,000-m depths near Axial in 2015, and $L = 260$ m, which is the minimum model horizontal cell size, criterion (1) is satisfied if

$$U << LN = 0.36 \text{ m/s.} \tag{2}$$

Therefore, the nonhydrostatic effects are not important at the spatial resolution employed in our model if the horizontal velocity associated with the downhill motions of brines is sufficiently small. Ultimately, a full evaluation of nonhydrostatic effects requires a direct comparison between the current simulation results and those obtained using a nonhydrostatic model. Such a comparison is beyond the scope of this study.

Lastly, the model brine sources are restricted to the areas along the 2015 dike that intruded Axial's summit assuming brines preferentially flow upward through the brecciated rocks near the dike walls. While this assumption is likely valid in layer 2B where the ambient crustal permeability is low, brines could flow through preexisting conduits away from the 2015 dike in layer 2A where the ambient crustal permeability is high. Therefore, it is possible that brines came out from broader areas than those occupied by the model sources. The locations of the southernmost model sources (inside box 2 in Figure 7b) follow the southward subsurface propagation of the 2015 dike, which overlaps the northern part of the 2011 eruption fissures (Figure 1b). It is possible that brines could come out from further south along the northern 2011 eruption fissures if the increased crustal permeability due to the intrusion of the 2011 dike in that region persisted until the 2015 eruption. Having a broader source distribution, especially a brine source closer to the two southernmost BPR sites: Int Dist and BPR-S2 would likely increase the spatial coherence of the model temperature anomalies and hence improve their match with the observations.

8.2. Justification of Model Heat and Salt Budgets

The total heat released in our best fit model simulation is 3.1×10^{16} J. This falls within the range of the estimated heat content of previously observed eruption-related megaplumes on the JdFR: 10^{16} to 10^{17} J (Baker et al., 1989). The amount of heat released in the model could result from venting of 1.8×10^7 m^3 of 350°C brines. This volume of brines could be hosted in a reservoir with a volume of 0.15 km^3 and a 12% porosity, which is the estimated global average of layer-2B porosity of zero-age crust (Canales et al., 2017). For example, such a subsurface volume could have physical dimensions of 70 m (35 m on either side of the dike) × 300 m (the vertical dimension) × 7,000 m (the length of the brine source in our model). The total amount of salt released in the model is 1.3×10^9 kg. To determine how long it will take this amount of salt to accumulate beneath Axial caldera, we assume the salt deficit of chronic venting that includes vapor and brine phase separation on Axial's summit is the dominant contributor to the storage of excess salt in the subsurface. Using 1,025 MW as the total heat flux from chronic venting on Axial's summit and 34% as the salinity deficit of vent fluids (D. Butterfield, personal communication), we estimate the current salt accumulation rate beneath Axial to be 1.5×10^8 kg/year. At this rate, it would take ~9 years to accumulate the amount of excess salt released in the model. This time scale is plausible, because there was no evidence for brine release after the 1998 and 2011 eruptions, and therefore, salt had possibly been accumulating beneath Axial caldera for at least 17 years before the 2015 eruption. Furthermore, as discussed in section 8.1, the amount of heat and salt needed to generate the observed 0.6°C to 0.7°C near-bottom temperature anomalies in the model are proportional to the bottom cell thickness in the model. If the vertical extent of the observed temperature anomalies were within 7 m of the bottom (instead of 13 m), then the amount of heat and salt from brines would be <50% of the aforementioned values. Likewise, the estimated salt accumulation time would reduce from 9 years to <5 years. In either case, the model heat and salt budgets needed to recreate temperature anomalies that are close to those observed are plausible.

8.3. Evaluation of Alternative and Preferred Hypotheses

In this study, we have considered four possible explanations for the temperature anomalies observed in and near the summit caldera of Axial Seamount during its 2015 eruption, which include (1) wide-spread eruption-related increase of diffuse venting, (2) warm plumes from the thickest 2015 northern lava flows, (3) warm plumes from Hawaiian-style fountaining during the 2015 eruption, and (4) release of a hydrothermal brine from below the caldera during the 2015 eruption. We have presented rebuttals to (1) and (3) (sections 4.1 and 4.3) and chosen (4) over (2) as our preferred hypothesis for the following reasons. The warm plume hypothesis requires a plume generated from the thickest NRZ lava flows to disperse at just the right depth (at the level of Axial's caldera), be transported in the right direction (southwestward from the NRZ toward Axial's summit), have sufficient size, and interact with the local circulation at Axial in a manner that allowed it to blanket the summit caldera for over a month. Among those requirements, we have only tested the first one using an integral plume model, whose results suggest that a plume from the NRZ lava flows with a temperature anomaly of 0.6–0.7°C could reach neutral buoyancy at the level of Axial's caldera if the source was >500-m deeper than the deepest northern lava flows discovered after the 2015 eruption or the source had a substantially higher salinity than ambient seawater. To test the other necessary conditions would require additional modeling to simulate the potential dispersion trajectories and patterns of a plume rising from a source near the NRZ lava flows in a realistic hydrodynamic environment, which is beyond the scope of this paper. Even if all the requirements were met, it is still uncertain whether the temporal pattern of the plume-induced near-bottom temperature anomalies would match the observations inside and near Axial's caldera. Nevertheless, it is important that future modeling studies be conducted to completely evaluate the feasibility of this hypothesis.

8.4. Implications for Hydrothermal Salinity Balance and Monitoring of Future Eruptions

There is evidence that some vent sites, such as the Main Endeavor Field on the Juan de Fuca Ridge, have vented fluids with salinities well below seawater for long periods of time (Butterfield et al., 1994). Such a salt deficit of chronic venting poses a question regarding the fate of brines produced by the phase separation in a subsurface hydrothermal circulation cell. Although there is strong evidence that brines are, at least temporarily, stored within the crust (Fontaine & Wilcock, 2006), how those brines are eventually removed from the crust is still not fully understood. Several mechanisms have been proposed to account for the *missing* brines. First, there is evidence that venting of brines occur at the final stage of a hydrothermal

system when its subsurface heat source is depleted (Choi & Lowell, 2015; Schoofs & Hansen, 2000). Second, some of the brines stored in the lower crust may be assimilated into axial magma chambers (Michael & Cornell, 1998). Lastly, the tidally driven subsurface mixing of brines with vapors (the low-salinity conjugate produced by phase separation) and the subsequent venting of the mixtures at the seafloor can be another mechanism for removing brines from the crust (Larson et al., 2009). If the temperature increases observed following the onset of the 2015 eruption of Axial Seamount were indeed caused by a release of brines stored in the crust, our model heat and salt budgets suggest the release would be sufficient to remove brines that had been accumulating from the chronic venting on Axial's summit for over a decade before the eruption. This suggests submarine eruptions or noneruptive dike intrusions could be an important and previously overlooked mechanism for the venting of brines stored in the subsurface.

While no salinity sensors were present in the caldera during the eruption to provide more conclusive evidence for the hypothesized brine release, the temperature observations and the evaluation of the hypothesis emphasize the importance of water-column observations during an eruption to better understand their impacts on hydrothermal systems. Those observations should not be restricted to near the seafloor but also include the water column to monitor the temperature, salinity, hydrodynamic, geochemical, and biological signals caused by an eruption. The OOI Cabled Array at Axial Seamount is an unprecedented platform that provides power and real-time data communication for a large number of scientific instruments. In preparation for the next eruption at Axial, it would be timely to augment the observatory with more instruments for water column measurements. As a first step, a seafloor CTD was funded by the National Science Foundation and deployed on the OOI Cabled Array in the ASHES vent field in July 2017 so that both temperature and salinity data will be available during the next eruption at Axial. In addition, a plan for deploying a resident autonomous underwater vehicle (AUV) for monitoring and tracking of water column eruption signals is currently under discussion (Manalang & Delaney, 2016).

9. Conclusions

The unusual temperature anomalies observed by cabled and autonomous instruments in and near the summit caldera of Axial Seamount during the 2015 eruption cannot be explained simply by the emplacement of lava flows on the seafloor nearby, because they differ substantially from those recorded during previous eruptions. After considering possible explanations, our preferred hypothesis is that the temperature increases were caused by the release of a warm, dense brine that had previously been stored in the crust. The modeling presented here shows that this hypothesis is at least plausible. If our interpretation is correct, this is the first time that the release of a hydrothermal brine has been observed due to a submarine eruption. This mechanism could provide a potential answer to a long-standing question regarding the fate of brines produced from phase separation of hydrothermal fluids, which is that submarine eruptions could be an important outlet for brines that accumulate in the crust from the salt deficit of chronic hydrothermal venting. Unfortunately, no salinity sensors were present in Axial caldera during the 2015 eruption to confirm the hypothesis. However, in response to the 2015 temperature signals and the development of this hypothesis to explain them, a seafloor CTD was funded by the National Science Foundation and deployed on the OOI Cabled Array in the ASHES vent field in July 2017. Therefore, during the next eruption at Axial Seamount there should be a salinity sensor in place in the caldera to directly test this brine release hypothesis.

References

Baker, E. T., Chadwick, W. W. Jr., Cowen, J. P., Dziak, R. P., Rubin, K. H., & Fornari, D. J. (2012). Hydrothermal discharge during submarine eruptions: The importance of detection, response, and new technology. *Oceanography*, *25*(1), 128–141. https://doi.org/10.5670/oceanog.2012.11

Baker, E. T., Lavelle, J. W., Feely, R. A., Massoth, G. J., Walker, S. L., & Lupton, J. E. (1989). Episodic venting of hydrothermal fluids from the Juan de Fuca ridge. *Journal of Geophysical Research*, *94*(B7), 9237–9250. https://doi.org/10.1029/JB094iB07p09237

Baker, E. T., Lupton, J. E., Resing, J. A., Baumberger, T., Lilley, M., Walker, S. L., & Rubin, K. (2011). Unique event plumes from a 2008 eruption on the Northeast Lau Spreading Center. *Geochemistry, Geophysics, Geosystems*, *12*, Q0AF02. https://doi.org/10.1029/2011GC003725

Baker, E. T., Massoth, G. J., & Feely, R. A. (1987). Cataclysmic hydrothermal venting on the Juan de Fuca ridge. *Nature*, *329*(6135), 149–151. https://doi.org/10.1038/329149a0

Baker, E. T., Massoth, G. J., Feely, R. A., Embley, R. W., Thomson, R. E., & Burd, B. J. (1995). Hydrothermal event plumes from the CoAxial seafloor eruption site, Juan de Fuca ridge. *Geophysical Research Letters*, *22*(2), 147–150. https://doi.org/10.1029/94GL02403

Bischoff, J. L., & Rosenbauer, R. J. (1989). Salinity variations in submarine hydrothermal systems by layered double-diffusive convection. *The Journal of Geology*, *97*(5), 613–623. https://doi.org/10.1086/629338

Butterfield, D. A., Jonasson, I. R., Massoth, G. J., Feely, R. A., Roe, K. K., Embley, R. E., et al. (1997). Seafloor eruptions and evolution of hydrothermal fluid chemistry. *Transactions of the Royal Society of London Series A*, *355*(1723), 369–386. https://doi.org/10.1098/rsta.1997.0013

Butterfield, D. A., Massoth, G. J., McDuff, R. E., Lupton, J. E., & Lilley, M. D. (1990). Geochemistry of hydrothermal fluids from axial seamount emissions study vent field, Juan de Fuca Ridge: Subseafloor boiling and subsequent fluid rock interaction. *Journal of Geophysical Research*, *95*(B8), 12,895–12,921. https://doi.org/10.1029/JB095iB08p12895

Butterfield, D. A., McDuff, R. E., Mottl, M. J., Lilley, M. D., Lupton, J. E., & Massoth, G. J. (1994). Gradients in the composition of hydrothermal fluids from the Endeavour segment vent field: Phase separation and brine loss. *Journal of Geophysical Research*, *99*(B5), 9561–9583.

Butterfield, D. A., Roe, K. K., Lilley, M. D., Huber, J., Baross, J. A., Embley, R. W., & Massoth, G. J. (2004). Mixing, reaction and microbial activity in sub-seafloor revealed by temporal and spatial variation in diffuse flow vents at Axial Volcano. In W. S. D. Wilcock, E. F. DeLong, D. S. Kelley, J. A. Baross, & S. C. Cary (Eds.), *The Subseafloor Biosphere at Mid-Ocean Ridges*, *Geophys. Monogr. Ser.*, (Vol. 144, pp. 269–289). Washington, DC: American Geophysical Union. https://doi.org/10.1029/144GM17

Canales, J. P., Carbotte, S. M., Nedimović, M. R., & Carton, H. (2017). Dry Juan de Fuca slab revealed by quantification of water entering Cascadia subduction zone. *Nature Geoscience*, *10*(11), 864.

Cann, J. R., & Strens, M. R. (1989). Modeling periodic megaplume emission by black smoker systems. *Journal of Geophysical Research*, *94*(B9), 12,227–12,237. https://doi.org/10.1029/JB094iB09p12227

Caplan-Auerbach, J., Dziak, R. P., Haxel, J., Bohnenstiehl, D. R., & Garcia, C. (2017). Explosive processes during the 2015 eruption of Axial Seamount, as recorded by seafloor hydrophones. *Geochemistry, Geophysics, Geosystems*, *18*, 1761–1774. https://doi.org/10.1002/2016GC006734

Caress, D. W., Clague, D. A., Paduan, J. B., Martin, J. F., Dreyer, B. M., Chadwick, W. W. Jr., et al. (2012). Repeat bathymetric surveys at 1-metre resolution of lava flows erupted at axial seamount in April 2011. *Nature Geoscience*, *5*(7), 483.

Chadwick, J., Perfit, M., Ridley, I., Jonasson, I., Kamenov, G., Chadwick, W. W. Jr., et al. (2005). Magmatic effects of the Cobb Hotspot on the Juan de Fuca Ridge. *Journal of Geophysical Research*, *110*, B03101. https://doi.org/10.1029/2003JB002767

Chadwick, W. W. Jr., Nooner, S. L., Butterfield, D. A., & Lilley, M. D. (2012). Seafloor deformation and forecasts of the April 2011 eruption at Axial Seamount. *Nature Geoscience*, *5*(7), 474.

Chadwick, W. W. Jr., Paduan, J. B., Clague, D. A., Dreyer, B. M., Merle, S. G., Bobbitt, A. M., et al. (2016). Voluminous eruption from a zoned magma body after an increase in supply rate at Axial Seamount. *Geophysical Research Letters*, *43*, 12,063–12,070. https://doi.org/10.1002/2016GL071327

Chadwick, W. W. Jr., Clague, D. A., Embley, R. W., Perfit, M. R., Butterfield, D. A., Caress, D. W., et al. (2013). The 1998 eruption of Axial Seamount: New insights on submarine lava flow emplacement from high-resolution mapping. *Geochemistry, Geophysics, Geosystems*, *14*, 3939–3968. https://doi.org/10.1002/ggge20202

Chadwick, Jr., W.W., Nooner, S. L., (2015). Processed Bottom Pressure Recorder (BPR) data from uncabled instruments deployed at Axial Seamount on the Juan de Fuca Ridge (investigators William Chadwick and Scott Nooner). Integrated Earth Data Applications (IEDA). http://doi.org/10.1594/IEDA/322282.

Choi, J., & Lowell, R. P. (2015). The response of two-phase hydrothermal systems to changing magmatic heat input at mid-ocean ridges. *Deep Sea Research, Part II*, *121*, 17–30. https://doi.org/10.1016/j.dsr2.2015.05.005

Clague, D. A., Dreyer, B. M., Paduan, J. B., Martin, J. F., Chadwick, W. W. Jr., Caress, D. W., et al. (2013). Geologic history of the summit of Axial Seamount, Juan de Fuca Ridge. *Geochemistry, Geophysics, Geosystems*, *14*, 4403–4443. https://doi.org/10.1002/ggge.20240

Clague, D. A., Paduan, J. B., Caress, D. W., Chadwick, W. W. Jr., Le Saout, M., Dreyer, B. M., & Portner, R. A. (2017). High-resolution AUV mapping and targeted ROV observations of three historic lava flows at Axial Seamount. *Oceanography*, *30*(4), 82–99. https://doi.org/10.5670/oceanog.2017.426

Clague, D. A., Paduan, J. B., Dreyer, B. M., Chadwick, W. W. Jr., Rubin, K. R., Perfit, M. R., & Fundis, A. T. (2018). Chemical variations in the 1998, 2011, and 2015 lava flows from Axial Seamount, Juan de Fuca Ridge: Cooling during ascent, lateral transport, and flow. *Geochemistry, Geophysics, Geosystems*, *19*. https://doi.org/10.1029/2018GC007708

Crisp, J. A. (1984). Rates of magma emplacement and volcanic output. *Journal of Volcanology and Geothermal Research*, *20*(3-4), 177–211. https://doi.org/10.1016/0377-0273(84)90039-8

Driesner, T. (2007). The system H_2O–NaCl. Part II: Correlations for molar volume, enthalpy, and isobaric heat capacity from 0 to 1000 C, 1 to 5000 bar, and 0 to 1 XNaCl. *Geochimica et Cosmochimica Acta*, *71*(20), 4902–4919. https://doi.org/10.1016/j.gca.2007.05.026

Dziak, R. P., & Fox, C. G. (1999). The January 1998 earthquake swarm at Axial Volcano, Juan de Fuca Ridge: Hydroacoustic evidence of seafloor volcanic activity. *Geophysical Research Letters*, *26*(23), 3429–3432. https://doi.org/10.1029/1999GL002332

Dziak, R. P., Haxel, J. H., Bohnenstiehl, D. R., Chadwick, W. W. Jr., Nooner, S. L., Fowler, M. J., et al. (2012). Seismic precursors and magma ascent before the April 2011 eruption at Axial Seamount. *Nature Geoscience*, *5*(7), 478.

Embley, R. W., Chadwick, W. W. Jr., Clague, D., & Stakes, D. (1999). The 1998 eruption of Axial Volcano: Multibeam anomalies and seafloor observations. *Geophysical Research Letters*, *26*(23), 3425–3428. https://doi.org/10.1029/1999GL002328

Embley, R. W., Murphy, K. M., & Fox, C. G. (1990). High-resolution studies of the summit of axial volcano. *Journal of Geophysical Research*, *95*(B8), 12785–12,812. https://doi.org/10.1029/JB095iB08p12785

Fontaine, F. J., & Wilcock, W. S. D. (2006). Dynamics and storage of brine in mid-ocean ridge hydrothermal systems. *Journal of Geophysical Research*, *111*, B06102. https://doi.org/10.1029/2005JB003866

Fox, C. G. (1999). In situ ground deformation measurements from the summit of axial volcano during the 1998 volcanic episode. *Geophysical Research Letters*, *26*(23), 3437–3440. https://doi.org/10.1029/1999GL900491

Fox, C. G., Chadwick, W. W. Jr., & Embley, R. W. (2001). Direct observation of a submarine volcanic eruption from a sea-floor instrument caught in a lava flow. *Nature*, *412*(6848), 727.

Kelley, D., Delaney, J. R., & Juniper, S. K. (2014). Establishing a new era of submarine volcanic observatories: Cabling Axial Seamount and the Endeavour segment of the Juan de Fuca Ridge. *Marine Geology*, *352*, 426–450. https://doi.org/10.1016/j.margeo.2014.03.010

Larson, B. I., Lilley, M. D., & Olson, E. J. (2009). Parameters of subsurface brines and hydrothermal processes 12–15 months after the 1999 magmatic event at the Main Endeavor Field as inferred from in situ time series measurements of chloride and temperature. *Journal of Geophysical Research*, *114*, B01207. https://doi.org/10.1029/2008JB005627

Lavelle, J. W., & Thacker, W. C. (2008). A pretty good sponge: Dealing with open boundaries in limited-area ocean models. *Ocean Modelling*, *20*(3), 270–292. https://doi.org/10.1016/j.ocemod.2007.10.002

Lavelle, J. W., Thurnherr, A. M., Ledwell, J. R., McGillicuddy, D. J., & Mullineaux, L. S. (2010). Deep ocean circulation and transport where the East Pacific Rise at 9–10 N meets the Lamont seamount chain. *Journal of Geophysical Research*, *115*, C12073. https://doi.org/10.1029/2010JC006426

Levy, S., Bohnenstiehl, D. R., Sprinkle, P., Boettcher, M. S., Wilcock, W. S. D., Tolstoy, M., & Waldhauser, F. (2018). Mechanics of fault reactivation before, during, and after the 2015 eruption of axial seamount. *Geology*, *46*(5), 447–450. https://doi.org/10.1130/G39978.1

Lowell, R. P., & Germanovich, L. N. (1995). Dike injection and the formation of megaplumes at ocean ridges. *Science*, *267*(5205), 1804–1807. https://doi.org/10.1126/science.267.5205.1804

Marshall, J., Hill, C., Perelman, C. L., & Adcroft, A. (1997). Hydrostatic, quasi-hydrostatic, and nonhydrostatic ocean modeling. *Journal of Geophysical Research*, *102*, 5733–5752.

Manalang, D., & Delaney, J. R. (2016). Axial seamount-restless, wired and occupied: A conceptual overview of resident AUV operations and technologies. In OCEANS 2016 MTS/IEEE Monterey (pp. 1-7). IEEE.

McDougall, T. J., & Barker, P. M. (2011). Getting started with TEOS-10 and the Gibbs Seawater (GSW) oceanographic toolbox, 28pp., SCOR/IAPSO WG127, ISBN 978-0-646-55621-5.

Meyer, J. L., Akerman, N. H., Proskurowski, G., & Huber, J. A. (2013). Microbiological characterization of post-eruption "snowblower" vents at Axial Seamount, Juan de Fuca Ridge. *Frontiers in Microbiology*, *4*, 153. https://doi.org/10.3389/fmicb.2013.00153

Michael, P. J., & Cornell, W. C. (1998). Influence of spreading rate and magma supply on crystallization and assimilation beneath mid-ocean ridges: Evidence from chlorine and major element chemistry of midocean ridge basalts. *Journal of Geophysical Research*, *103*(B8), 18,325–18,356. https://doi.org/10.1029/98JB00791

Murton, B. J., Baker, E. T., Sands, C. M., & German, C. R. (2006). Detection of an unusually large hydrothermal event plume above the slow-spreading Carlsberg ridge: NW Indian Ocean. *Geophysical Research Letters*, *33*, L10608. https://doi.org/10.1029/2006GL026048

Nooner, S. L., & Chadwick, W. W. (2016). Inflation-predictable behavior and co-eruption deformation at Axial Seamount. *Science*, *354*(6318), 1399–1403. https://doi.org/10.1126/science.aah4666

NSF Ocean Observatories Initiative, Data Portal (2016). http://ooinet.oceanobservatories.org, Bottom pressure Tilt (RS03CCAL-MJ03F-BOTPTA301, RS03ECAL-MJ03E-BOTPTA302, RS03INT2-MJ03D-BOTPTA303) data from 16 September 2014 to 20 May 2016.

Rubin, K. H., Soule, S. A., Chadwick, W. W. Jr., Fornari, D. J., Clague, D. A., Embley, R. W., et al. (2012). Volcanic eruptions in the deep sea. *Oceanography*, *25*(1), 142–157. https://doi.org/10.5670/oceanog.2012.12

Sasagawa, G. S., Cook, M. J., & Zumberge, M. A. (2016). Drift-corrected seafloor pressure observations of vertical deformation at Axial Seamount 2013–2014. *Earth and Space Science*, *3*(9), 381–385. https://doi.org/10.1002/2016EA000190

Schoofs, S., & Hansen, U. (2000). Depletion of a brine layer at the base of ridge-crest hydrothermal systems. *Earth and Planetary Science Letters*, *180*(3-4), 341–353. https://doi.org/10.1016/S0012-821X(00)00184-9

Speer, K. G., & Rona, P. A. (1989). A model of an Atlantic and Pacific hydrothermal plume. *Journal of Geophysical Research*, *94*(C5), 6213–6220. https://doi.org/10.1029/JC094iC05p06213

Spietz, R. L., Butterfield, D., Buck, N. J., Larson, B., Chadwick, W. W. Jr., Walker, S., et al. (2018). Deep-sea volcanic eruptions create unique chemical and biological linkages between the subsurface lithosphere and oceanic hydrosphere. *Oceanography*, *31*(1), 128–135. https://doi.org/10.5670/oceanog.2018.120

Tao, Y., Rosswog, S., & Brüggen, M. (2013). A simulation modeling approach to hydrothermal plumes and its comparison to analytical models. *Ocean Modelling*, *61*, 68–80. https://doi.org/10.1016/j.ocemod.2012.10.001

Turner, J. S., & Campbell, I. H. (1987). Temperature, density and buoyancy fluxes in "black smoker" plumes, and the criterion for buoyancy reversal. *Earth and Planetary Science Letters*, *86*(1), 85–92. https://doi.org/10.1016/0012-821X(87)90191-9

Wilcock, W. S., Tolstoy, M., Waldhauser, F., Garcia, C., Tan, Y. J., Bohnenstiehl, D. R., et al. (2016). Seismic constraints on caldera dynamics from the 2015 Axial Seamount eruption. *Science*, *354*(6318), 1395–1399. https://doi.org/10.1126/science.aah5563

Xu, G., & Di Iorio, D. (2012). Deep sea hydrothermal plumes and their interaction with oscillatory flows. *Geochemistry, Geophysics, Geosystems*, *13*, Q0AJ01. https://doi.org/10.1029/2012GC004188

Xu, G., & Lavelle, J. W. (2017). Circulation, hydrography, and transport over the summit of Axial Seamount, a deep volcano in the Northeast Pacific. *Journal of Geophysical Research: Oceans*, *122*, 5404–5422. https://doi.org/10.1002/2016JC012464